Cu-doped and un-doped WO3 photochromic thin films

Yazan Badour, Sylvain Danto, Christine Labrugère, Mathieu Duttine, Manuel Gaudon

Cu-doped and un-doped WO_3 photochromic thin films

Yazan Badour, Sylvain Danto, Christine Labrugère, Matthieu Duttine, Manuel Gaudon*

Received 00th January 20xx,

Accepted 00th January 20xx

DOI: 10.1039/x0xx00000x

0, 0.5, 1, 2% Cu-doped WO_3 nanoparticles were synthesized via polyol method. The as-synthesized materials have been characterized by X-ray diffraction, scanning electron microscopy (SEM), electron paramagnetic resonance (EPR), X-ray photoelectron (XPS) and UV-VIS photochromic activity. A bond valence model was adapted to explain the relationship between the lattice parameter and Cu percentage. Moreover, two films (1% Cu-doped and un-doped samples) obtained by dip-coating from a well dispersed suspension have been optically investigated using *ex-situ* and *in-situ* UV-Vis spectrometry: colouring/bleaching kinetics have been thoroughly studied. The Cu-doped WO_3 film has been recorded with a high quality bleaching mechanism (5 times faster than the un-doped WO_3 film). Finally, the high bleaching performance of the doped films has been confirmed by successive cycling showing the as-prepared compounds are of great interest besides smart windows application, for illustration.

1. Introduction

Tungsten oxide compounds (WO_x) have been intensively investigated over the last decades due to their large variety of structures giving rise to great potential applications such as photo-chromic optical devices, gas sensors, photocatalyst, flat panel displays, and in field emission [1][2][3]. WO_3 is an n-type indirect bandgap semiconductor with an optical bandgap ranging from 2.7 to 3.25 eV, which allows UV-light absorption [4]. Pristine WO_x based materials have a good photochromic behavior but this intrinsic property has several limitations including its limited applicable wavelength range, poor reversibility, and low photoresponse kinetic [5][6]. Because of these drawbacks, considerable attention was made towards composite inorganic materials due to their improved performances based on synergistic effects [7]. In another approach, doping the WO_3 crystalline structure with typical elements like Al, Cu, Mo, Zn, Co, etc was investigated [8][9][10]. It has been proved to decrease the oxide bandgap and especially, by introducing a narrow electronic band between the CB and the VB, has been shown to be able to tune the photochromic UV-irradiation response. Recently in 2021, Dong's group has conducted a detailed study on the effect of Cu doping on the photochromic properties of Cu@h-WO_3/WO_3·nH_2O hierarchical microsphere composites where the self-bleaching process was shown to be greatly accelerated upon increasing the Cu doping concentration [11]. Shen *et al.* [12] found that the WO_3 photochromic behavior was highly improved by Al^{3+} upon the formation of W_2O_5 which induced an electronic transition band between the VB and CB of WO_3, generating red shift of the gap values and leading to a prominent promotion of the photochromic performance of WO_3. Also, the electronic, catalytic and optical performance of WO_3 can be enhanced by refining oxide crystallite size and chemical purity [13]. Thus, diverse chemical synthesis methods were adapted for preparing pure nano-WO_3 including hydrothermal [14], sol–gel [15] and polyol methods [16].

Univ. Bordeaux, CNRS, Institut de Chimie de La Matière *Condensée de Bordeaux, UMR 5026, F-33600, Pessac, France.*
**manuel.gaudon@icmcb.cnrs.fr*

As it was reported in our previous work [17], the as-prepared WO_{3-x} nanoparticles (NPs) by polyol method have improved chemical, morphological, structural, and optical properties, such as improved photochromic behavior. Hitherto, it encouraged us to conduct a detailed photochromic (coloring or bleaching cycles) study on thin films obtained by dip-coating from non-stoichiometric WO_{3-X} NPs in suspension [18]. In this latest study, we have found that the photochromism phenomenon was based on two kinetic components, the photoreduction of W^{6+} ions in W^{5+} defects at the particle surfaces and the diffusion of the W^{5+} species within the bulk of the particles, which led to a coloration mechanism from the W^{5+}-W^{6+} intervalence charge transfer. Regardless of the improved optical contrast, the time necessary for a complete return seems very long and needs to be improved. Hence this limitation triggered us to search for another way to develop the photochromic performance of WO_{3-X} NPs based materials. In this frame, we propose in this article to study the photochromic behavior of Cu-doped WO_3 thin film obtained by dip-coating Cu-doped WO_{3-x} NPs dispersed in ethanol suspensions. In the first part, the discussion focuses on the effect of the different concentrations of Cu (0.5, 1 and 2 mol%) introduced in the WO_{3-x} NPs prepared by the polyol method. In a second part, the photochromic (coloring and bleaching) behaviors of the doped and pristine films are compared and deeply analyzed.

2. Experimental

2.1. Polyol synthesis of WO_3 powders

Chemical reagents were purchased from Sigma Aldrich and used as received. Tungsten (VI) chloride was used as tungsten source, copper (II) chloride as doping source and diethylene glycol (DEG) as solvent. WCl_6 (7.2 g) was added to 100 mL of DEG and 20 mL of distilled water. The mixture was heated at 180°C under continuous stirring and refluxed for 3 h. At the end of the reaction, a deep blue precipitate was obtained. The precipitate was washed and centrifuged several times with ethanol to remove any traces of solvent and dried in an oven at 80°C before being washed in HCl solution (1 mol. L^{-1}) for surface functionalization with protons.

In this way, a series of Cu-doped-WO_3 samples were prepared while varying Cu concentration from 0%, 0.5%, 1%, 2% and have been labeled as WO, WCu05, WCu1, and WCu2, for raw powders respectively. In another batch, the as-synthesized powders (0%, 0.5%, 1%, 2% Cu) were annealed at 600°C under air atmosphere for 2 hours and have been labeled as WOT, WCuT05, WCuT1, and WCuT2, respectively.

2.2. Pristine and doped films elaboration

The Pristine WO and WCu1 raw NPs were separately dispersed in ethanol to prepare the suspensions (weight content in NPs is 90 $g.L^{-1}$); then the suspensions are dip-coated on standard glass substrate to obtain pristine and doped thin films. The dip-coating parameters are (i) dip-coating speed: 133 $mm.min^{-1}$ and (ii) for multilayers, the successive dip-coating steps which are operated with between two steps a 30 min drying in an oven (90°C).

2.3. Characterization techniques

2.3.1 Powder Characterization

The crystal structure information of the products was analyzed by X-ray diffraction analysis (PAN analytical X'Pert Pro instrument Cu $K_{\alpha1}$ = 1.54056 Å, $K_{\alpha2}$ = 1.54439 Å and 2θ range from 8° to 80°). The unit cell parameters were refined by structural pattern matching using the Fullprof program package. The surface morphologies of the samples were investigated by scanning electron microscopy (Quanta 3D FEG) working at 5 kV acceleration voltage.

To detect Cu^{2+} ($3d^9$) and W^{5+} ($5d^1$) paramagnetic ions and/or free electrons in the conduction band of the tungsten trioxide semi-conductors, electron paramagnetic resonance (EPR) experiments were performed on powder samples. EPR spectra were recorded from room temperature down to 4 K with a Bruker ESP300E spectrometer equipped with a liquid helium flow cryostat. 9.54 GHz (X-band) microwaves with 50 mW power and a 100 kHz magnetic field modulation with 0.5 mT amplitude were used for these experiments. The magnetic field (and *g*-value) scale was calibrated with a DPPH((2,2)-diphenyl-1-picrylhydrazyl; *g* = 2.0036) reference sample. The analysis of the EPR spectra were performed with Bruker WinEPR and WinSimFonia softwares.

The optical properties of the resulting products were tested by the UV–VIS diffuse reflectance spectroscopy at room temperature from 200 to 2000 nm using Cary 5000 s using an integration sphere (spectral resolution: 1 nm and band length: 2 nm) . Halon was used as white reference. RGB space colorimetric parameters were determined from the spectra using a two-step mathematic treatment. The first step consists in extracting the XYZ tri-stimulus values (defined by the CIE, 1964) from the integration (over the visible range, i.e. from λ = 380 nm up to 780 nm) of the product of x(λ), y(λ) or z(λ) functions (CIE – 1964) with the diffuse reflectance spectra function $X = \int x(\lambda).R(\lambda).d\lambda$. Then, we used the transfer equations defined by the CIE, 1976, to transform the XYZ space to the L*, a* and b* common three-color space parameters.

A ThermoFisher Scientific K-ALPHA spectrometer was used for XPS surface analysis with a monochromatized Al K_α source (hν = 1486.6 eV) and a 400 microns X-Ray spot size. A pressure of 10-7 Pa was reached in the chamber when transferring the powders pressed onto indium foil. The full spectra (0-1100 eV) were obtained with constant pass energy of 200 eV and high resolution spectra with constant pass energy of 40 eV. Charge neutralization was applied during analysis. High resolution spectra (*i.e.* C1s, O1s, W4f) were quantified and/or fitted using the AVANTAGE software provided by ThermoFisher Scientific.

2.3.2. Films Characterization

Dynamic light scattering (DLS) was used to determine the size distribution profile of the pristine and doped NPs in the suspensions used for dip coating process with a VASCO™ nanoparticle size analyser. Films Transmission spectra were recorded at room temperature from 200 to 2500 nm on a Cary 5000 spectrophotometer. The irradiation conditions were accomplished using a UV Hg-lamp (Vibert Lourmat 8.LC) at a monochromatic wavelength of 365 nm. The film was placed at 10 cm from 8 W tubes: the power per surface unit received by the sample is equal to 5.6 W/m^2, i.e. irradiance close to the UV-daylight irradiance in London daylight. The use of such low fluence is to mimic the real condition a smart device (window or textiles) is exposed to a daily light. Self-bleaching occurred naturally after samples were placed in a dark room away from light. Finally, the thickness of the films was determined using a WYCO NT1100 optical profilometer.

3. Results and Discussion

3.1. Powder physico-chemical characterizations

The structure of the as-prepared powders was characterized by X-ray diffraction. No second phase corresponding to impurities such as Cu, Cu_2O or CuO was detected in the X-ray patterns associated to all the samples. The XRD diagrams show that all raw powders: WO, WCu05, WCu1 and WCu2, have crystallized with a cubic Pm-3m structure (Fig.1a) [17] and on Fig.1b the powders obtained after a post-annealing under air, with a P21/n monoclinic structure. The very large peaks associated with the nanometric behavior of the raw powders do not allow their fitting for accurate structural characterization. Thus, to determine the impact of the copper content introduction inside the WO_3 crystalline framework, especially on crystallite size and the unit-cell lattice parameters, pattern-matching refinement of the air-annealed powders was performed on Fig.1b. The pattern matching of the air-annealed samples can be achieved using the P21/n space group. The matching quality is good, and the reliability factors are far below 10%: for illustration, Rexp = 2.16%; Rf = 6.55%; Rp = 8.47% for the WOT compound. From the diffraction pattern peak profiles, it is possible to determine the average crystal size of the particles with the help of Debye-Scherrer formula [19], $t = K.\lambda / (\beta.\cos\Theta)$ with *t* the mean size of the ordered (crystalline) domains, which may be smaller or equal to the particle size, *K* the proportionality factor (also called the Scherrer's constant), which value is often assumed to be *K* = 0.9, β the full width at half maximum (FWHM), λ the X-ray wavelength and θ the Bragg angle. It should be noted that the observed peak width is affected by the instrumental broadening as well as the broadening caused by the size effect (size broadening), so the instrumental broadening is subtracted to the total peak width to calculate the crystallite size.

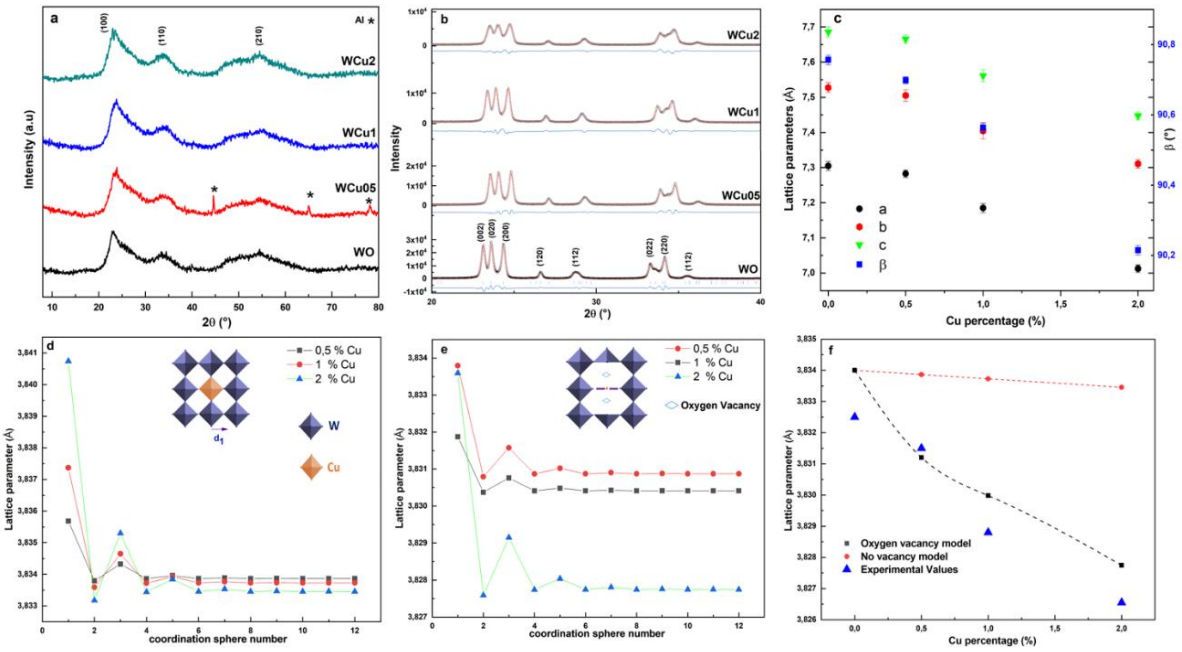

Figure 1. XRD pattern of undoped and Cu-doped WO_3 raw powders (a). XRD with pattern matching refinement for of undoped and Cu-doped WO_3 annealed powders under air at 600°C (b). Evolution of undoped and Cu-doped WO_3 annealed powders lattice parameters as a function of Cu dopant percentage (c). Calculation of the Cu doping effect on the Cu-doped WO_3 pseudo-cubic lattice parameter considering W^{6+} for Cu^{2+} substitution without electronic compensation versus length of the coordination spheres number around copper taken for calculation (d). W^{6+} for Cu^{2+} substitution with double oxygen vacancies creation for electronic compensation (e). Calculated and experimental lattice parameter values (f).

The calculated nanometric sizes were obtained equal to (i) 5.5, 3.2, 3.5, 2.6 nm for WO, WCu05, WCu1,and WCu2 respectively, (ii) 25.6 , 22.34 ,19.8 , 21.8 nm for WOT, WCuT05, WCuT1, and WCuT2 respectively. The copper doping leads so, especially for the post-annealed samples, to a decrease of the average particle size, which argues for an efficient introduction of the copper ions inside the WO_3 crystalline framework. As shown in Fig.1b, the decrease of the crystallite size is associated to the decrease of the intensity of major diffraction peaks such as (020), (002) and (200) with increasing of Cu concentration. This trend can be a result of the formation of the copper ion clusters and crystal defects which can limit the growth of the Cu-coped WO_3 NPs [20]. Furthermore, the incorporation of Cu ions into the WO_3 crystal affected the lattice parameters of Cu-doped WO_3 as the Cu^{2+} ions and W^{6+} ions have different ionic radius which are 7.3 and 6.0 Å in 6-coordinated spheres, respectively, as well as different oxidation states (aliovalent doping). One can notice that Rietveld refinement performed on Cu-doped samples did not reveal any electronic residues in interstitial position (for illustration in the icosahedral sites, which are known to be preferential locations for alkaline dopants in WO_3-type framework [21]). Hence, in the following, the copper ions are considered in substitution for the tungsten ones. Additionally, the copper oxidation states are supposed to be +II, which will be supported by further EPR experiments.

As illustrated in Fig.1c, further analysis on the monoclinic lattice parameters (*a*, *c* and *β* angle) of Cu-doped samples shows a clear and monotonic decreasing trend as the Cu doping concentration increases. This observation could constitute an interesting paradox as the Cu^{2+} ionic radius is over the W^{6+} radius. The evolution of the unit-cell lattice parameters has been interpreted in respect with the bond valence model [22].

However, two different approaches have been applied to better understand the evolution of the Cu-doped WO_3 lattice parameters upon doping with Cu. First, for simplification, the evolution of the unit-cell parameters was resumed to the pseudo-cubic *a* unit-cell parameter (considering the equivalent cubic cell with Z, the number of WO_3 unit per cell, equal to unity). In a rough model, in a first approximation, a pseudo-cubic lattice parameter was calculated taking into consideration a W^{6+} for Cu^{2+} substitution without electronic compensation. In a more accurate model, the creation of a double oxygen vacancy creation for electronic compensation is taken into account. For the calculation, the two oxygen vacancies are created along the z-axis, in first neighboring of the introduced copper ions, i.e., considering that copper II ions are so located in a regular square plane sites (in good agreement with the $3d^9$ Cu^{2+} electronic configuration).

In both approaches, the bond-valence model of Brown *et al*. [22] was used to predict from a geometrical modelling the drastic modifications of the W-O interatomic distances around the Cu^{2+} defect points. Indeed, the bond valence law expresses that the bond length (r_i), the coordination number (n), the electronic flux on each bond (v_i) and the ion oxidation state (or total ion valence: V) are both linked by the Equation 1:

$$V = \sum_{i=0}^{n} v_i = \sum_{i=0}^{n} \exp((r_0 - r_i)/0.37) \qquad \text{Eq.1}$$

Where V is the valence of the ion (equal to the oxidation degree modulus: here = 6 for W^{+6}, 2 for Cu^{2+}), v_i is the bond valence of each bond implying the central ion, r_0 is an empirically determined parameter characteristic of the A–X bond (r_0 is tabulated equal to 1.917 Å, and 1.679 Å for Cu^{2+}–O^{2-}bond), and r_i is the length of each i bond of the first coordination sphere.

This model is very adequate to explain that an aliovalent doping by a low valence but bigger radius ion could paradoxically lead to a decrease of the unit-cell parameters, exactly as observed for Cu-doped WO_3 samples. Indeed, even if the Cu-O bonds are longer than the standard W-O bonds, the increase of the electronic flux of the W-O bonds at the proximity of the copper defect leads to a contraction of these W-O bond lengths. Indeed, it is mandatory for the surrounding crystalline network around the copper defect to compensate the low electronic flux between oxygen and copper, because of the total valence equal to 2 of the Cu-bonded oxygen anions must still constant.

In addition, we use the Vegard law (i.e., a mixing law) to evaluate the lattice parameter taking into account the valence bond modification from neighbor to near-close bond fluxes up to the tenth coordination sphere from copper ions [23]. For the first model, the lattice parameter remains the same for all the three axes, whereas in the second model, for which a double oxygen vacancy (V_O) was introduced along the z axis, the lattice parameter on z axis a_z differs from the x and y axes ($a_x = a_y \neq a_z$). Then the average calculated pseudo-cubic unit-cell parameter a is taken as $a = (a_x \,.\, a_y \,.a_z)^{1/3}$. Thus, for both the first and the second model, a pseudo cubic parameter for *x* copper concentration (n being the number of coordination spheres around copper taken in the model) can be calculated from Equations 2 and 3. The two models are diverging in the way to calculate near-close bond fluxes.

$$a_n = 2.d_{(W\text{-}O)}(1\text{-}2x)+2.x.d_{(Cu\text{-}O)}+\sum_{i=0}^{i=n} 2.x.d_i \qquad \text{Eq.2}$$

$$\text{with } d_i = r_{0(W/Cu\text{-}O)} - 0.37.\ln(v_i) \qquad \text{Eq.3.}$$

The final calculation for both models is represented in Fig.1d and Fig 1.e, respectively for non-vacancy approximation, and double oxygen vacancy approximation. The second applied model is in good accord with the experimental values which confirms that substituting W^{6+} by Cu^{2+} causes a decrease of the lattice parameters and leads to shrinkage of the unit cell. The fact that the second model leads to calculation so close to the experimental values tend to validate that compensation of copper doping with a double oxygen vacancy is the convenient way to testify the evolution of lattice parameters.

The sample morphologies are reported in the SEM images in Fig.2. As shown in Fig.2a-d, the raw sample particles are very small with a size around 3 nm. The crystallite size distribution extracted from SEM image treatment is reported in Fig.1i. All the doped and un-doped NPs have almost a superimposed particle size distribution. This very small size is in good agreement with the previous discussion extracted from the X-ray diffraction patterns. The air-annealed powders show significantly larger isotropic particles of about 50 nm average diameters (Fig.2e-h). However, the doped NPs did not exhibit change in their morphology and size distribution in comparison with the un-doped NPs. The coherent domain decrease with the copper concentration shown from X-ray patterns is not confirmed. May, the slight enlargement of the peak width versus copper content observed in X-ray diffraction comes more from constrains created from copper introduction than from a decrease of the average crystallite size. While the monoclinic samples were deeply analyzed in terms of X-ray diffraction technique to confirm the substitution of tungsten cation for copper due to their well-defined X-ray diffraction patterns, in the following of the study, we will focus on raw-powders, these latter samples being the only one exhibiting the target photochromic properties.

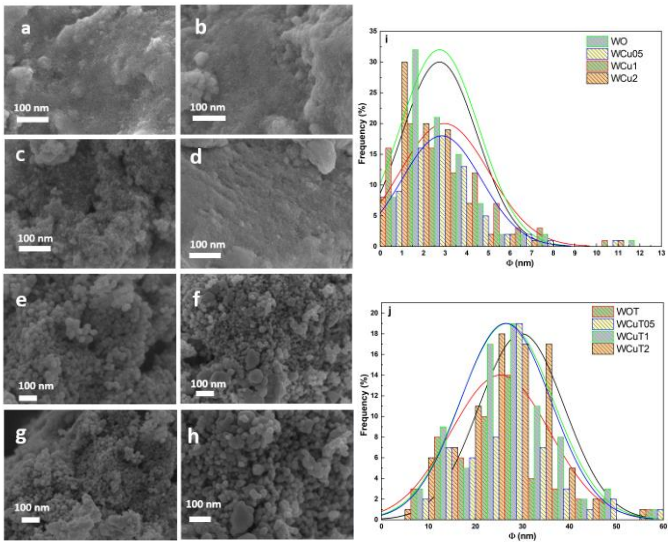

Figure 2. SEM images of the various raw and post-annealed samples: WO (a), WCu05 (b), WCu1 (c), WCu2 (d), WOT (e), WCuT05 (f), WCuT1 (g), WCuT2 (h) and their associated particle size distribution (i & j).

In order to reveal the occurrence of conduction electrons and to track the variation in Cu^{2+} and W^{5+} content within the studied products, EPR experiments were performed from room temperature down to 4 K (Fig. 3). First, no conduction electron, responsible for a sharp and intense signal with *g* factor close to free electron *g* value ($g_e = 2.0023$), was detected in all the analyzed samples. However, the EPR spectra of Cu-doped WO_3 powders mainly exhibit an axial signal ($g_\perp = 2.085$ and $g_{//} = 2.42$) with a hyperfine structure ($A_\perp \approx 2$ mT and $A_{//} = 12$ mT) whose intensity increases linearly with the Cu-doping rate. This EPR signal with $g_{//} > g_\perp > g_e = 2.0023$ is characteristic of $3d^9$ Jahn-Teller Cu^{2+} ions ($S = 1/2$ and $I = 3/2$ for ^{63}Cu and ^{65}Cu isotopes) located in tetragonally distorted octahedra (D_{4h} local symmetry). Clearly, the experiment shows that copper is well introduced in the WO_3-type crystalline structure and with mainly the +II oxidation number. Nevertheless, the presence of copper ions at a lower oxidation state may not be rejected as diamagnetic Cu^+ ($3d^{10}$) is EPR silent. Moreover, low-temperature EPR spectra show at higher magnetic field two additional signals associated with $5d^1$ W^{5+} ions (Fig. 3). These apparently axial signals (inset of Fig. 3) with *g* values $g_{zz} = 1.82$, $g_{yy} = 1.80$, $g_{xx} = 1.76$ and $g_{zz} = 1.77$, $g_{yy} = 1.74$, $g_{xx} = 1.69$ can be related to slightly different local environment for 5-fold coordinated W^{5+} ions (with a symmetry close to C_{4v}) and then to the occurrence of oxygen vacancies within all the analyzed samples. The presence of W^{5+} ions in the raw powder can be easily explained by the reducing medium used during the polyol synthesis route, which result in an oxygen sub-stoichiometry with chemical formulae WO_{3-x}. Versus copper concentration, two observations can be made on W^{5+} signals: (i) the intensity of the signal is progressively decreasing, showing that copper insertion plays an oxidative role besides tungsten ions; (ii) the ratio between the two W^{5+} signals clearly evolves, showing the perturbation of the W^{5+} local environments.

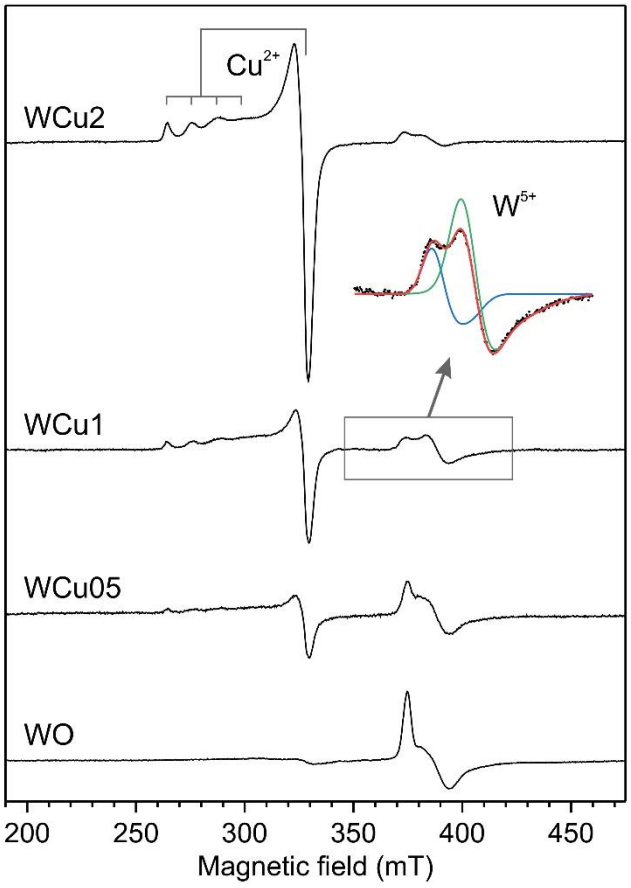

Figure 3. Low temperature (4 K) X-band EPR spectra of undoped and Cu-doped WO_3 raw powders. The inset highlights the two distinct EPR signals associated with two different local environments for W^{5+} ions.

XPS was used to analyse the surface composition as a coupling and complementary analysis technique to EPR. Indeed, a clear picture of the tungsten oxidation states can be achieved whereas EPR was obviously non-sensitive to the W^{6+} diamagnetic cations. Furthermore, the environment of the oxygen anions in the powders, especially the ability to distinguish oxygen anions in bulk environment from the ones perturbed by oxygen vacancies is very useful for materials understanding.

Firstly, the XPS spectra of two air-annealed compounds, the un-doped (WO) and the 2 mol% Cu-doped sample (WCuT2) are compared. Fig. 4a shows that the air annealing post-treatment produces the full oxidation of the tungsten ions up to the +VI oxidation state in the WOT samples. Indeed, the WOT spectrum is constituted only by two peaks which were assigned without any doubt to W^{6+} state ($4f_{5/2}$ and $4f_{7/2}$ doublet at 38.0 eV and 35.9 eV) [26]. This sample is so a reference demonstrating that no further reduction of W^{6+} to W^{5+} is occurring during the XPS spectrum acquisition. However, the W_{4f} fitting of the air annealed WCuT2 shows a residual signal of W^{5+}. The W^{5+} doublet, $4f_{5/2}$ - $4f_{7/2}$: 36.8 - 34.6 eV, confirms the substitution of tungsten ions by the Cu^{2+}. Indeed, W^{5+} may be created from a redox reaction proceeded from intervalence electronic transfer between W^{6+} and Cu^{2+} cations to lead to W^{5+} and Cu^{+} cations. Also, the occurrence of W^{5+} inside the WCuT2 compound is in coherence with the green colour of the annealed powder comparing to the yellow colour of the un-doped WOT powder.

The next other spectra are all dealing with un-doped or doped raw powders. Fig.4c shows the high-resolution fitting of W_{4f} spectra in the pure WO sample where the two major peaks were assigned to W^{6+} while the two minor peaks were assigned to W^{5+} cation. The W^{5+} state occurrence indicates the creation of oxygen vacancies as a result of a partial reduction of W^{6+} due to the reducing medium used during the polyol synthesis, as reported in our last paper [27]. Therefore, the un-doped tungsten oxide NPs have an oxygen sub-stoichiometry with the formula: WO_{3-x}.

Similarly, the fitting of W_{4f} spectra for each of the raw Cu-doped WO_{3-x} samples revealed two W^{6+} and W^{5+} doublets [29]. Nevertheless, the ratio between the tungsten V and tungsten VI peaks is clearly decreasing versus the copper concentration. Hence, W^{5+} content in WO sample is calculated from $W4f_{7/2}$ peak area ratio, to be equal to 0.19 and was found to be decreased to 0.14 and 0.11 in WCu1 and WCu2, respectively.

For all the powders, the high-resolution O1s spectra were fitted with four components to bring supplementary information. As shown in Fig.4f, g, h, the strongest signal at 530.7 eV corresponds to the oxygen atoms contained in the stoichiometric structure of WO_3 [29], i.e., introduced in a well-defined 6-coordinated oxygen site. The second signal (531.7 eV) is related to the existence of oxygen defects in the sub-surface planes of the powders. The signal at 532.7 eV corresponds to oxygens bound to carbon atoms, which could come from the synthesis route (polyol-mediated precipitation), and the signal at 533.3 eV is attributed to water pollution. Interestingly, the peak intensity of O_{1s} state relative to oxygen defects (located at 531.7 eV) shows a significant increase upon Cu doping increase. This leads to an estimation of the oxygen vacancy (V_O), estimated from the O_{1s} 531.8 / O_{1s} 530.7 area ratio, content equal to 0.12 in the un-doped sample, and to 0.24, 0.32 in WCu1, WCu2, respectively. This last observation so indicates a drastic increase in the oxygen vacancies in WO_{3-x} after Cu doping which could be due to the aliovalent character of the chemical doping. Indeed, the drastic difference in the valence state of Cu ion in regard with the host W ions of the matrix should be electronically compensated from oxygen vacancies. This observation is in good agreement with the variation of the unit-cell parameters versus copper concentration which were discussed previously.

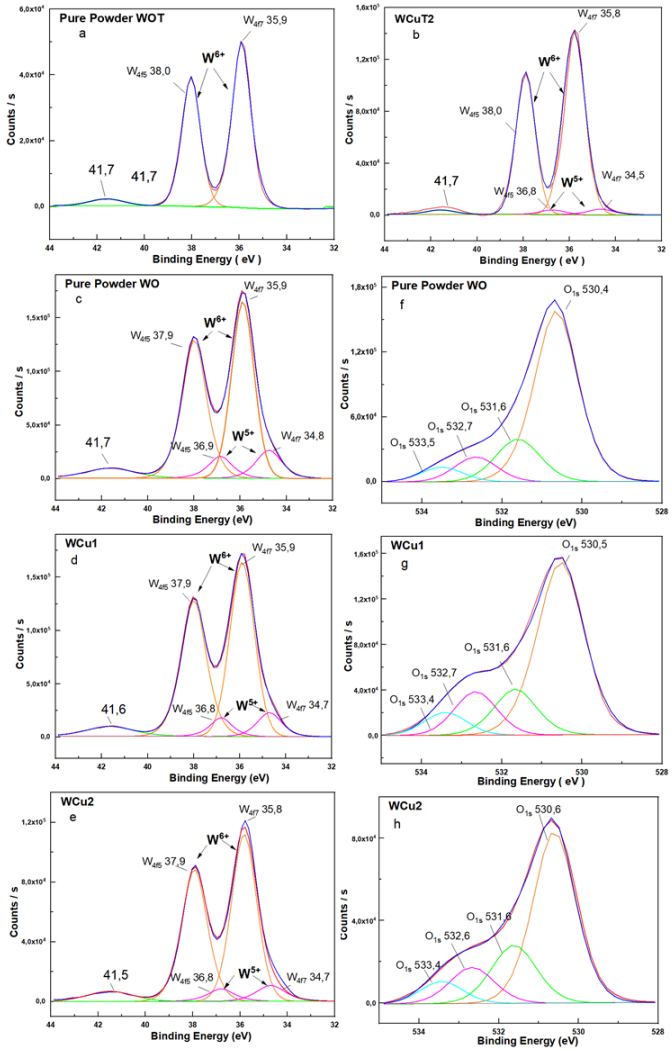

Figure 4. High resolution XPS spectra of W_{4f} (a up to e) and O1s (f, g, h) in WOT (a), WCuT2 (b). WO (c and f), WCu05 (d and g), WCu2 (e and h).

3.2. Powder photochromic properties

The optical photochromic response of the as-prepared powders under UV irradiation was studied on the whole UV-visible-NIR range by measuring the diffuse reflectance spectra of un-doped and doped raw powders. All samples were characterized before UV irradiation and after 5 min irradiation as shown in Fig.5.

Firstly, the doped and un-doped powders possess a fully total absorption in the UV, i.e., typically characteristic of a wide-gap semiconductor, with the gap being located at 420 nm for the un-doped and shifted to 485 nm for doped powder. Furthermore, a quite important absorption in the visible and the near infrared part of the spectrum is due to the inter-valence charge transfers between W^{5+} and W^{6+} or even can be described from the creation of the free charge carriers in the conduction band associated with the reduction of tungsten ions as explained by the Drude electronic cloud theory [7]. For the non-irradiated compounds, the infrared absorption increases with the copper concentration. Because the W^{5+} ion concentrations was shown to decrease with the copper concentration, the increase of the intervalence transfer probability with copper supports the participation of the copper to electronic mobility: the occurrence of multi-site charge transfers as in the short chains: W^{5+} - Cu^{2+} - W^{6+} → W^{6+} - Cu^{+} - W^{6+} → W^{6+} - Cu^{2+} - W^{5+}, can explained the phenomenon. Nonetheless, the oxygen sub-stoichiometry linked to the copper defects, as it was confirmed by the XPS results, can also be at the origin of the absorption of more photons of the visible energy range. The maximum of reflectivity percentage located at 480 nm decreases from 35% for the raw sample, to 30% for the WCu05, to 17% for the WCu1, and 10% for the WCu2. As shown from the sample photographs as well as the reconstructed sample colorations from their L*, a*, b* colorimetric coordinates, the color of samples become darker upon increasing of copper concentration.

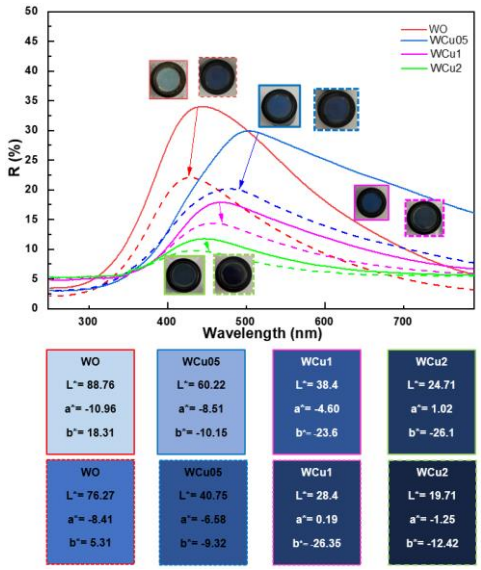

Figure 5. Diffuse reflectance spectra of the undoped and Cu-doped WO_3 raw powders and their associated L, a*, b* parameters before irradiation (solid line) and after 10 min UV irradiation (dashed line).*

Irrespective of their copper doping attribute all the samples exhibit a huge photochromism in comparison with previous investigations reported on WO_3 photochromism [17][18]. This behavior is related to the nanometric crystallite sizes. Indeed, thermodynamically, the relaxation of the steric constrains linked to the photoreduction promoting the creation of new W^{5+} color centers, would preferentially take place on oxide surfaces. Highly divided materials will then show improved photochromic properties.

The associated chromatic coordinates in L*, a*, b* space presented in Fig.5 allow the comparison of the photochromic efficiency of the various samples from the optical contrast calculated between the non-irradiated and 10 min. irradiated samples. Indeed, even if our samples exhibit a photochromic effect mainly concentrated in the near-infrared part of the spectrum, the impact of the intervalence transfers in the visible range allows the observation of visible $\boldsymbol{\Delta C}$ contrast: $\boldsymbol{\Delta C} = \sqrt{(\boldsymbol{\Delta b^{*2}} + \boldsymbol{\Delta L^{*2}} + \boldsymbol{\Delta a^{*2}})}$. Photochromic contrasts are about 55.5, 50.6 25.6 and 20.1 for WO, WCu05, WCu1 and WCu2, respectively. From the darkening of the non-irradiated

compounds versus copper concentration, the copper introduction tends so to decrease the powder photochromic efficiency in terms of optical contrast between bleached and colored states.

3.3. Thin film photochromic properties

Next part devoted to the elaboration from powder to thin films and the characterization of its photochromic properties is focused on the comparison between the un-doped tungsten oxide (WO) thin film and the 1 mol% Cu-doped WO_3 (WCu1) thin film.

The elaboration of thin films of good quality requires the elaboration of well-dispersed colloidal suspensions. DLS measurements were used to track the size variation of the 90 $g.L^{-1}$ dispersed NPs in suspension. Fig.6a shows that powder in ethanol suspension with a Gaussian particle size distribution from the WOCu1 powder (similar curve is obtained for the WO powder) centered on an average size equal to 23 nm is obtained from the adequate protocol already experimented in previous work [18]. The suspension remained stable with no sedimentation observed over time.

Different films issued from successive dip-coating steps (with 1, 2, 3 or 4 successive coated layers) have been studied. The transmission spectra of as-prepared thin films show a good visible transmission with a very low scattering coefficient (Fig.6b). The films show a maximum transmission equal to 80 % at 600 nm, irrespective of the film thickness. However, a distinct low-intensity absorption band appearing at a wavelengths around1200 nm is observed on the 3- and 4-layer films. This absorption band can be without any doubt attributed to the presence of W^{5+} ions due to the intervalence charge transfer (IVCT) between W^{5+} and W^{6+} ions in the crystal network of the WO_{3-x}. The film thickness is plotted versus the number of deposited layers in Fig.6c. The variation of the film thickness versus the number of coating layers is almost linear: about 100 nm thickness is achieved for each coating.

A preliminary photochromic test with fixed irradiation conditions (UV lamp, 8 W, 30 min.) has been conducted on all studied films. A focus is made on the 3-layer film since significant IVCT transfer in the NIR-region is observed; these preliminary tests have shown that UV-irradiation well generates the photochromism effect. Therefore, the evolution of the spectrum of both WO and WCu1 films versus irradiation time was collected (Fig.7a and 7b) and the evolution of the absorbance at 1.1 eV for WO films and 0.75 eV for WCu1 film is extracted to investigate further the photo-redox kinetic (Fig.7c). As shown in Fig.7a or 7b, the initial absorbance of the films (before UV-irradiation) was considered as the reference absorbance (without any absorbance).

As seen from Fig.7c, the absorbance at 1 eV (corresponding to the energy at which the IVTC band is the greater) of WO film seems changing rapidly in the first minutes of irradiation, then seems slowing down beyond 15 min of irradiation until almost no longer evolving after 90 min. In turn, the absorbance of WCu1 seems changing slower than the WO in the first minutes of irradiation, then stabilizes after 90 min. Also, the absorbance band maximum is shifted at 0.75 eV. This change of position of the absorbance phenomenon is coherent with the participation of the Cu^{2+} to the IVCT (W^{6+} to W^{5+} via Cu^{2+} ions in intermediate positions) as proposed mechanism to explain the darkening of the pristine oxide coloration before irradiation. To better express the differences between both films, a double exponential function (a combination of two first-order kinetic laws) was used to fit the experimental data (absorbance evolution at its maximum), according to the Equation 4:

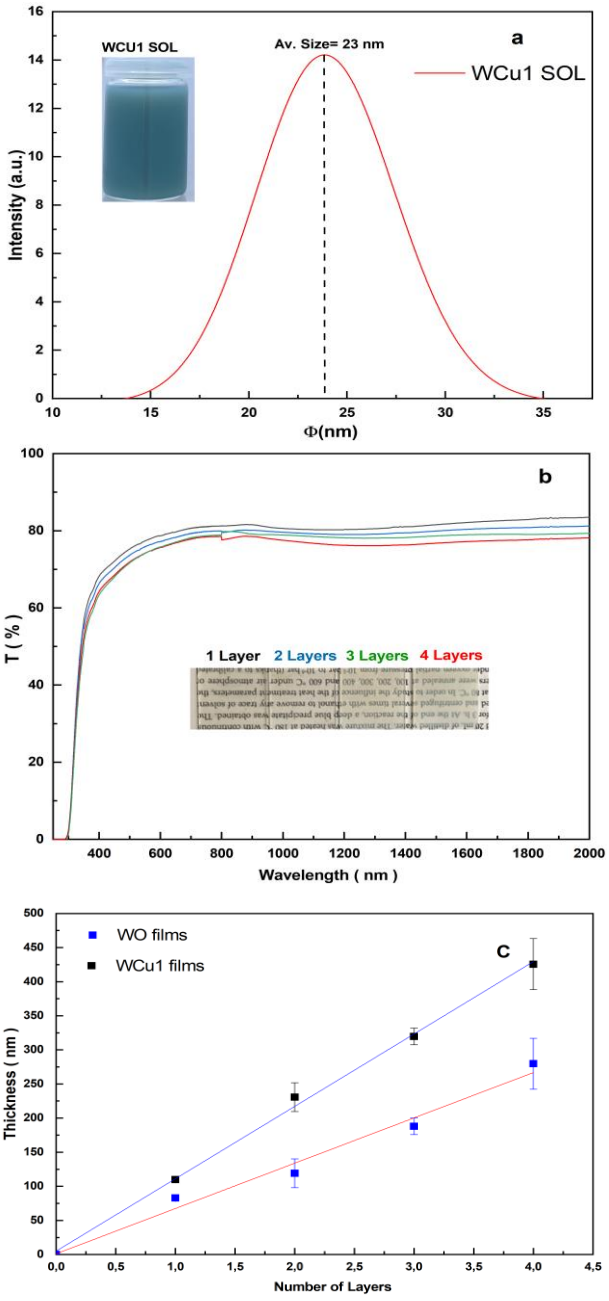

Figure 6. Particle size distribution of WCu1 NPs in ethanol suspension (a), Transmission spectra and photographs of WCu1 films issued from 1 up to 4 successive dip-coated layers (b), Evolution of raw and doped film thickness as function of number of dip-coated layers (c).

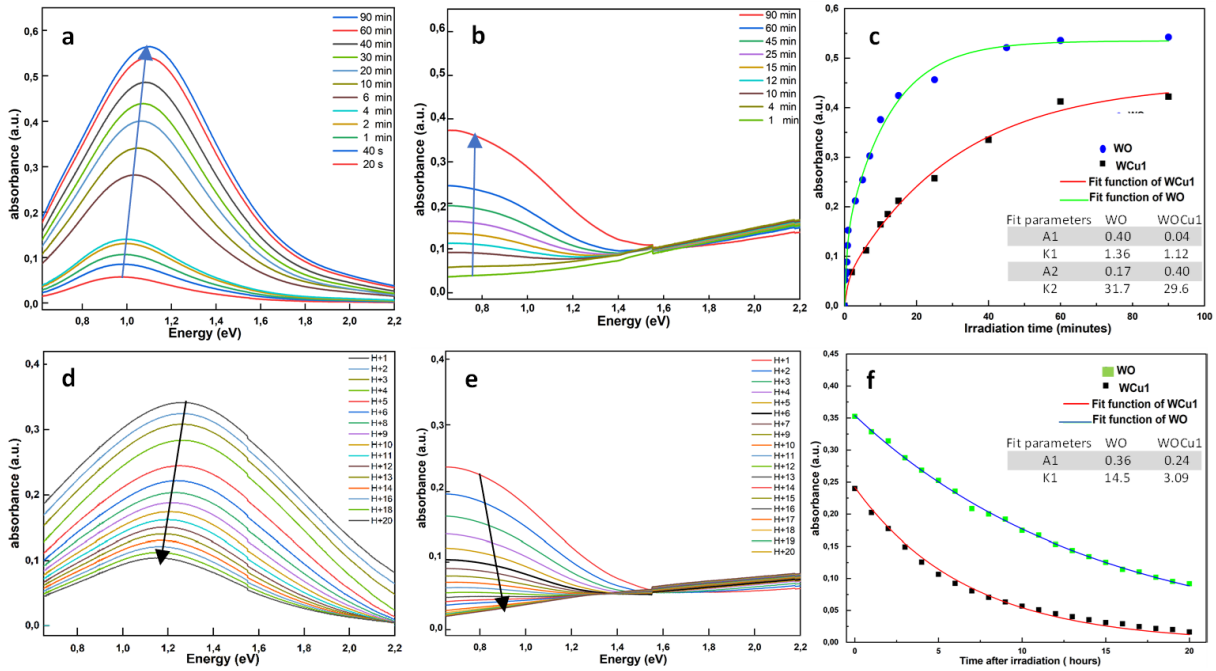

Figure 7. Evolution of absorbance during irradiation (coloring) of WO film (a), WCu1 film (b). For both films, absorbance at 1 eV (WO) or 0.75 eV (WCu1) evolution versus irradiation time and the associated kinetic parameters (coloring kinetic) (c). Evolution of absorbance in dark conditions (bleaching) of WO film (d), WCu1 film (e). For both films, absorbance evolution at 1 eV (WO) film or 0.75 eV (WCu1) in dark conditions (bleaching kinetic) (f).

$$Y = A_1.[1-\exp(-t/k_1)\ ] + A_2.[1-\exp(-t/k_2)\ ] \qquad \text{Eq.4}$$

With *t* in min., and so two characteristic times (k_1 and k_2) in min., and two characteristic amplitudes (A_1 and A_2). The values of the four parameters are shown in Fig.7c. For both films, the coloring kinetic consists in two convoluted kinetic phenomena: a fast-kinetic component (k_1 is about 1 minute), and a slow-kinetic component (k_2 is about half an hour). Hence, in both cases (doped or un-doped thin films): (i) the fast kinetic (during the very first minutes) could correspond to a quick photo-reduction of the surface cations from W^{+6} to W^{+5} then, the surface after a short time will be saturated with W^{+5} ions and this fast mechanism stop; the slow kinetic could correspond to the ionic diffusion of the W^{5+} from the surface to the material bulk, allowing W^{5+} surface desaturation and so new surface photoreduction. Nonetheless, a huge difference is observed comparing the doped and un-doped film: while on the un-doped WO film, the coloring under UV irradiation is mainly governed by the fast kinetic phenomenon (A_1 = 0.4 whereas A_2 = 0.17), the WCu1 film coloring is mainly governed by the diffusive slow kinetic (A_1 = 0.0.4 whereas A_2 = 0.4). The quasi-quenching of the fast kinetic takes origin in the defects associated to the Cu-doping. Basically, when Cu atom takes the W site in WO_3, it produces three possible effects: (a) the narrowing of the fundamental band gap of the system due to the strong d–p coupling between Cu and O, which in turn leads O 2p level up, (b) the creation of an acceptor impurity narrow band above the valence band of WO_3 which is formed by the empty Cu 3d (e_g) orbital, (c) the creation of electronic compensating oxygen vacancies as bulk/surface defect [31][30]. Thus, upon irradiation, after the appearance of electron/hole pairs which are generated at conduction band minimum (CBM) and valence band maximum (VB), respectively, then non-radiative recombination can be amplified from these defects. For illustration, Cu^{2+} can easily captures the electron to become Cu^{+} with full-filled electronic structure, resulting in a by-pass of the W^{6+} to W^{5+} photoredox mechanism. In other illustration, a segregation of the compensating oxygen vacancies at the surface avoids the valence band's holes/oxygen recombination required to close the photoredox process.

For the bleaching properties, one can first notice that many research groups reported that the bleaching kinetic is very slow for tungsten oxide based materials. Self-bleaching (when the product is only left in a dark environment to relax) is even most of the time not observed at all, i.e. it is often necessary to heat the film at 80°C-100°C in air or under ozone (oxidative conditions) to obtain a complete relaxation [2] [32]. In our case, the 3-layers WO and WCu1 films which were previously irradiated for 45 min (to nearly gain the coloring saturation) and let in dark at room temperature for self-bleaching, show a photochromic reversibility. The bleaching study was performed in the spectrometer chamber (dark condition) to record the evolution of the transmission spectra: a spectrum analysis is automatically performed every hour for 20 hours, stopping the sample illumination at 500 nm in order to produce any electron/hole pair creation. The absorbance spectra are shown in Fig.7d and 7e for WO and WCu1, respectively.

Bleaching evolution was followed recording the absorbance at 1eV for the WO film and at 0.75 eV for the WCu1 film, in agreement with previous studies. First, for the WO films, the residual absorbance at 1 eV obtained after 20 hours darkening is still important: equal to about 0.3, whereas the bleaching is total for the WCu1 film, absorbance equal to 0.02 (Fig.7f). The absorbance evolution for both films can be fitted from a single exponential decay trend on the whole 20 first hour's range. The single exponential decay function to fit the experimental data, according to the Equation 5, with t and k in hours, is:

$Y = A_1.[1-\exp(-t/k_1)]$ Eq.5

Comparing both films (Fig.7f), the speed of the bleaching mechanism in WCu1 is almost five times faster than for the WO film: k = 3.09 and 14.05 hours, respectively. Thus, copper greatly improved the photochromic reversibility.

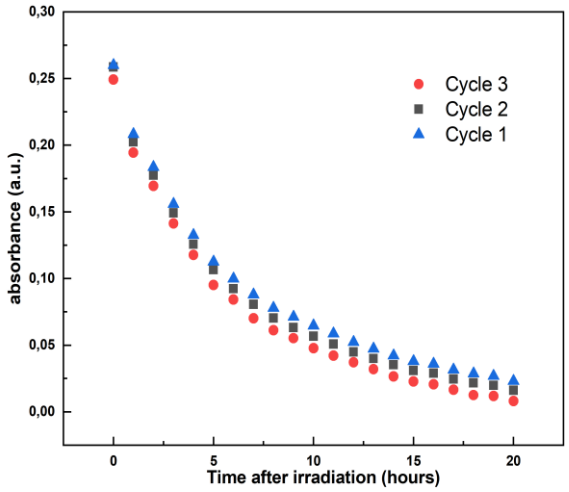

Figure 8. WCu1 film absorbance evolution at 0.75 eV versus darkening time through three successive coloring/bleaching cycles.

Finally, the great bleaching properties observed on copper doped WO_3 film has allowed cycling tests to be performed. Cycling tests were carried out on the WCu1 film as depicted in Fig.8. Several irradiation steps were applied for 45 min irradiation, with sufficient darkening duration (15 hours, i.e. very near a night & day real cycling conditions) in between each the irradiation steps to let the compound fully self-bleached. The results show that the three cycles are almost identical which confirm the strong stability of the films under successive cycling and this augurs to be able to apply such thin films as smart windows for environmental buildings.

Briefly, in WO film, the phenomenon of re-oxidation of W^{5+} to W^{6+} by the oxygen in the air is very slow resulting in a long bleaching time. This represents a severe restriction for large scale application of such thin films as smart window photochromic films. In WCu1 film, the enhancement in photochromic reversibility, *i.e.* with a drastic increase of the bleaching kinetic, was ascribed to several factors, based on the characterization results. Notably, the increase in oxygen vacancies in WO_3 after Cu doping could extend the light-harvesting ability to the visible and near-infrared region. Also, the double injection mechanism added to the improved electron interactions thanks to the existence of W^{6+}, W^{5+}, Cu^{+} and Cu^{2+} ions, surely plays a significant role in the bleaching improvement. The "de-trapping" of color center electrons created on 5d tungsten orbitals during UV irradiation thanks to an additional, new W^{5+} - Cu^{2+} → W^{6+} - Cu^{+} intervalence electronic transfer is proposed. Furthermore, the energetic proximity of the copper 3d (e_g) level and oxygen 2p levels, favoring p-d coupling, can further lead to close the photoredox loop through the recombination of the defect electron trapped as Cu^{+} defect above the valence band and the hole created in the maximum of the VB band during irradiation.

Conclusion

In conclusion, doping of WO_3 with Cu prepared by polyol method has been proved to be an effective strategy to improve the bleaching mechanism of our studied films. The photochromism (coloring/bleaching) kinetic of these composites was thoroughly studied. The coloring mechanism of un-doped films governed mainly by fast component consists of quick photo-reduction of the surface cations from W^{+6} to W^{+5}. Then the surface after a short time becomes saturated with W^{+5} ions and this fast mechanism stop. On the contrary, the WCu1 film kinetic, which is governed by the slow component, corresponds to the ionic diffusion of the W^{5+} from the surface to the material bulk. The WCu1 film records a faster bleaching with an order of 3.09 hours comparing to 14.05 hours for the WO film. The bleaching kinetic was enormously enhanced due to the increase in oxygen vacancies in WO_3 after Cu doping, which could in turn extend the light-harvesting ability of this compound to the visible and near-infrared region. In addition, the cycling study on WCu1 film confirms the efficiency of the product in optical application. This study is a proof of the promising usability of our films in different optical applications such as smart textile, smart window or optical filters.

Conflicts of interest

There are no conflicts to declare.

References

1. F. Cora, M. Stachiotti, C.R.A Catlow and C.O. Rodriguez, Journal of Physical Chemistry A, Transition Metal Oxide Chemistry: Electronic Structure Study of WO_3, ReO_3, and $NaWO_3$, 1997, 101, 3945–3952.
2. J. Wei, X. Jiao, T. Wang and D. Chen, Electrospun Photochromic Hybrid Membranes for Flexible Rewritable Media, ACS Applied Material Interfaces, 2016, 8, 29713–29720.
3. R. Diehl, G. Brandt and E. Salje, The crystal structure of triclinic WO_3, Acta Crystallographica, 1978, 34, 1105–1111.
4. Y.S. Zou, Y.C. Zhang, D. Lou and H.P. Wang, Structural and optical properties of WO_3 films deposited by pulsed laser deposition, Journal Alloys Compounds, 2014, 583, 465–470.
5. N. Li, Y. Zhao, Y. Wang, Y. Lu, Y. Song, Z. Huang, Y. Li, and J. Zhao, Aqueous Synthesis and Visible-Light Photochromism of Metastable h-WO_3 Hierarchical Nanostructures, European Journal of Inorganic Chemistry, 2015, 2804–2812.
6. C.S. Blackman and I.P. Parkin, Atmospheric Pressure Chemical Vapor Deposition of Crystalline Monoclinic WO_3 and WO_{3-x} Thin Films from Reaction of WCl6 with O-Containing Solvents and Their Photochromic and Electrochromic Properties, Chemistry of Materials, 2005, 17, 1583–1590.
7. S.K. Deb, Opportunities and Challenges in Science and Technology of WO_3 for Electrochromic and Related Applications, Solar Energy Materials and Solar Cells, 2008, 92, 245-258.
8. C.O. Avellaneda and L.O.S. Bulhones, Photochromic Properties of WO_3 and WO_3:X (X=Ti, Nb, Ta and Zr) Thin Films, Solid State Ionics, 2003, 165, 117– 121.
9. O. Oderinde, M. Kang, M. Kalulu, F. Yao and G. Fu, Facile Synthesis and Study of the Photochromic Properties of Deep Eutectic Solvent-Templated Cuboctahedral-WO_3/MoO_3 Nanocomposites, Superlattices and Microstructures, 2018, 125, 103–112.
10. V. Hariharan, V. Aroulmoji, K. Prabakaran B. Gnanavel, M. Parthibavarman, R. Sathyapriya and M. Kanagaraj, Magnetic and Electrochemical Behaviour of Cobalt Doped Tungsten Oxide (WO_3) Nanomaterials by Microwave Irradiation Method, Journal of Alloys and Compounds, 2016, 689, 41-47.

11. X. Dong. Z. Wu, Y. Guo, Y. Tong, X. Liu, L. Zhang and Y.Lu, Rational Modification in the Photochromic and Self-Bleaching Performance of Hierarchical Microsphere Cu@h-WO_3/WO_3·nH_2O Composites, Solar Energy Materials and Solar Cells, 2021, 219, 11078.
12. Y. Shen, P. Yan, Y. Yang, F. Hu, Y. Xiao, L. Pan and Z. Li, Hydrothermal Synthesis and Studies on Photochromic Properties of Al Doped WO_3 Powder, Journal of Alloys and Compounds, 2015, 629, 27–31.
13. M. Sun , N. Xu , Y. W. Cao , J. N. Yao and E. G. Wang , Preparation, Microstructure and Photochromism of a New Nanocrystalline WO_3 Film, Journal of Materials Science Letters, 2000, 19, 1407-1409.
14. D.J. Ham, A. Phuruangrat, S. Thongtem and J.S. Lee, Hydrothermal Synthesis of Monoclinic WO_3 Nanoplates and Nanorods Used as an Electrocatalyst for Hydrogen Evolution Reactions from Water, Chemical Engineering Journal, 2010, 165, 365–369.
15. X. Sun, H. Cao, Z. Liu and J. Li, Influence of Annealing Temperature on Microstructure and Optical Properties of Sol-Gel Derived Tungsten Oxide Films, Applied Surface Science, 2009, 255, 8629.
16. H. Dong, Y. Chen and C. Feldmann, Polyol Synthesis of Nanoparticles: Status and Options Regarding Metals, Oxides, Chalcogenides, and Non-Metal Elements, Green Chemistry, 2015, 17, 4107–4132.
17. M. Bourdin, M. Gaudon, F. Weill, M. Duttine, M. Gayot, Y. Messaddeq and T. Cardinal, Nanoparticles (NPs) of WO_{3-x} Compounds by Polyol Route with Enhanced Photochromic Properties, Nanomaterials, 2019, 9, 1555.
18. M. Bourdin, G. Salek, A. Fargues, S. Messaddeq, Y. Messaddeq, T. Cardinal and M. Gaudon, Investigation on the Coloring and Bleaching Processes of WO_{3-x} Photochromic Thin Films, Journal of Materials Chemistry C, 2020, 8, 9410-9421.
19. R. Gross and A. Marx, "Festkörper physic" 3rd Edition, Hubert & Co. GmbH & Co. KG, Göttingen, 2018.
20. J.B. Lee, H.J. Le, S.H. Seo, and J.S. Park, Characterization of Undoped and Cu-Doped ZnO Films for Surface Acoustic Wave Applications, Thin Solid Films, 2001, 398, 641-646.
21. Z. Wang, X. Fan, D. Hana and F. Gu, Structural and Electronic Engineering of 3DOM WO_3 by Alkali Metal Doping for Improved NO_2 Sensing Performance, Nanoscale, 2016, 8, 10622-10631.
22. I.D. Brown, "The Chemical Bond in Inorganic Chemistry" Oxford University Press, Oxford, U.K., 2002.
23. A.R. West, "Solid State Chemistry and its Applications", 2nd Edition, John Wiley & Sons, 1991.
24. A. Goldstein, V. Chiriac and D. Becherescu, On some d^1 Ions Spectra in Oxide Glasses, Journal of Non-Crystalline Solids, 1987, 92, 271–277.
25. D. Möncke, J. Jiusti, L.D. Silva and A.C.M. Rodrigues, Long-Term Stability of Laser-Induced Defects in (Fluoride-)Phosphate Glasses Doped with W, Mo, Ta, Nb and Zr Ions, Journal of Non-Crystalline Solids, 2018, 498, 401–414.
26. H.Y. Wong, C.W. Ong, R.W.M. Kwok, K.W. Wong, S.P. Wong and W.Y. Cheung, Effects of Ion Beam Bombardment on Electrochromic Tungsten Oxide Films Studied by X-Ray Photoelectron Spectroscopy and Rutherford Back-Scattering, Thin Solid Films, 2000, 376, 1311-39.
27. M. Bourdin, I. Mjejri, A. Rougier, C. Labrugere, T. Cardinal, Y. Messaddeq and M. Gaudon, Nano-Particles (NPs) of WO_3-Type Compounds by Polyol Route with Enhanced Electrochromic Properties, Journal of Alloys and Compounds, 2020, 823, 153690.
28. T.H. Fleisch and G.J. Main, An XPS Study of the UV Reduction and Photochromism of MoO_3 and WO_3, Journal of Chemical Physics, 1982, 76, 780-786.
29. J. Diaz-Reyes, R. Castillo-Ojeda, M. Galvan-Arellano and O. Zaca-Moran, Characterization of WO_3 Thin Films Grown on Silicon by HFMOD, Advances in Condensed Matter Physics, 2013, 591787.
30. N. Kadam, T.G. Kim, D.S. Shin, K.M. Garadkar and J. Park, Morphological Evolution of Cu Doped ZnO for Enhancement of Photocatalytic Activity, Journal of Alloys and Compounds,2017, 710, 102–113.
31. B.M. Alshabander, Copper(II)-Doped WO_3 Nanoparticles with Visible Light Photocatalytic Antibacterial Activity Against Gram-Positive and Gram-Negative Bacteria, Inorganic and Nano-Metal Chemistry, 2020, 2470-1556.
32. S. Wang, W. Fan, Z. Liu, A. Yu and X. Jiang, Advances on Tungsten Oxide Based Photochromic Materials: Strategies to Improve their Photochromic Properties, Journal of Materials Chemistry C, 2018, 6, 191–212.